Redox behavior of the SOFC electrode candidate NdBaMn2O5+: δ investigated by high-temperature in situ neutron diffraction: First characterisation in real time of an Ln BaMn2O5.5 intermediate phase

F. Tonus, M. Bahout, V. Dorcet, G.H. Gauthier, Serge Paofai, R.I. Smith, S.J. Skinner

Redox behavior of the SOFC electrode candidate $NdBaMn_2O_{5+\delta}$ investigated by high-temperature *in situ* neutron diffraction: first real-time characterisation of an *Ln*$BaMn_2O_{5.5}$ intermediate phase

Florent Tonus[1], Mona Bahout[2], Vincent Dorcet[2], Gilles H. Gauthier[3], Serge Paofai[2], Ronald I. Smith[4], and Stephen J. Skinner[1*]*

[1] Department of Materials, Imperial College London, Exhibition Road, London SW7 2AZ, United Kingdom.
[2]Institut des Sciences Chimiques de Rennes, UMR CNRS 6226, Université de Rennes 1, 263 Avenue du Général Leclerc, 35042 Rennes, France.
[3]Universidad Industrial de Santander, Grupo INTERFASE, Carrera 27, Calle 9, Ciudad Universitaria, Bucaramanga, Colombia.
[4]The ISIS Facility, STFC Rutherford Appleton Laboratory, Harwell Campus, Didcot, OX11 0QX, UK.

ABSTRACT

The structural behavior of $NdBaMn_2O_5$, a member of the family of *A*-site ordered layered manganites that have been recently suggested as possible mixed ionic and electronic conductors, has been investigated by means of *in situ* neutron powder diffraction (NPD). Considering applications in energy production and storage devices, the study was carried out in relevant atmosphere conditions, *i.e.* dilute hydrogen (wet and dry) and dry air in the temperature range 25-800 °C. Neutron data allowed for the first time under flowing hydrogen in a double perovskite manganite, *i.e.* $NdBaMn_2O_5$, monitoring of the structural phase transition from the charge-ordered to the charge disordered state as a function of temperature. Slow reduction kinetics of the fully oxidised phase, $NdBaMn_2O_6$, previously formed from quick oxidation of the pristine material, enabled the observation and real-time crystal characterization *in operando* of the intermediate phase, $NdBaMn_2O_{5.5}$ with an orthorhombic unit cell ~ 4 times larger than the tetragonal P_4/nmm parent phase, $NdBaMn_2O_5$. Oxygen vacancy ordering within the Nd layers of $NdBaMn_2O_{5.5}$ correlated to antiferrodistortive orbital ordering of the Mn^{3+} ions in the square pyramids and octahedra retained at high temperature results in large thermal expansion and relatively slow anisotropic oxygen diffusion occurring in the NdO layer. The four heating/cooling cycles evidenced no oxygen miscibility between the three phases detected in the $NdBaMn_2O_{5+\delta}$ system and clearly demonstrated that topotactic oxygen intercalation/deintercalation underpins the stability of the

Ln$BaMn_2O_{5+\delta}$ materials to redox cycling and to wet atmosphere in high temperature electrochemical devices.

Keywords: electrode, Symmetrical SOFC, ordered manganites, *in situ* neutron diffraction, charge/orbital ordering, redox cycling, $NdBaMn_2O_{5.5}$

1. Introduction

The development of new energy technologies has become important with the present situation of increasing energy demand, rising energy prices, and reinforcement of countermeasures for global warming and its detrimental climatological, ecological, and sociological effects. During the last decades, Solid Oxide Fuel Cell (SOFCs) have been considered an interesting alternative for sustainable energy generation, as they can operate either with hydrogen, a non-polluting fuel or with any hydrocarbon-based fuel, fossil or synthetic, with potential for producing electricity more efficiently than conventional power generation like technologies[1, 2]. In particular, the Ni-YSZ cermet (YSZ = yttria-stabilized zirconia), widely used as the SOFC anode, exhibits poor redox cycling stability: Ni is easily deactivated by oxidation to NiO, nickel coarsens after prolonged operation causing poor electronic conduction, and the anode suffers from coking and sulphur poisoning contamination when hydrocarbon fuels are used[3]. In the most serious circumstances, the electrode fails mechanically as a result of deposited coke or re-oxidation[4]. Consequently, redox stability and reversibility have been emphasised as important requirements for the fuel electrode material in SOFCs and Solid Oxide Electrolyser cells (SOECs).

Recently, a particular class of double perovskite manganites, *Ln*$BaMn_2O_{5+\delta}$ (*Ln* = lanthanide), in which the Ln^{3+} and Ba^{2+} cations order in alternating layers, have drawn considerable attention as electrode materials for SOFCs and SOECs as well as having potential as oxygen storage materials[5-9].

In particular, the manganite, $PrBaMn_2O_{5+\delta}$ was found to be stable both as SOFC anode withstanding sulfur contamination and carbon deposition when operating on direct hydrocarbons[10] and as a SOEC cathode for high temperature electrochemical CO_2 electrolysis[11]. Furthermore, the structurally related

$NdBaMn_2O_{5+\delta}$ compound was shown to be a potential electrode material for symmetrical SOFCs[12]. In such a configuration the same electrode material is used as both anode and cathode, with significant advantages compared to traditional configurations regarding both fabrication and maintenance/operation. In this work, we used high temperature *in situ* neutron powder diffraction to monitor the structural and redox behaviors of $NdBaMn_2O_{5+\delta}$ under 5% H_2/He (dry and wet) and dry air flows.

2. Experimental

Powder of $NdBaMn_2O_{5+\delta}$ (~ 5 g) was prepared *via* the citrate-nitrate synthesis route using Nd_2O_3, $BaCO_3$ and MnO as starting materials, all Sigma Aldrich with a purity of 99.99%. Nd_2O_3 was heated at T ~ 800 °C overnight and $BaCO_3$ was treated at T ~ 550 °C for 1 h prior to weighing to remove adsorbed moisture. Stoichiometric quantities of the metal oxides or carbonates were added to 100 mL of distilled water in a beaker containing nitric acid and citric acid. The quantity of nitric acid was such that the metal oxides or carbonates transformed to nitrates. The molar ratio of citric acid/total metal ions was fixed at 2:1. The solution was heated to 50 °C to allow the dissolution to proceed to completion. Ammonia solution (30 wt. %) was added to maintain the pH at 7 in order to improve the efficiency of the self-combustion reaction. The temperature was increased gradually up to ~ 300 °C under continuous stirring until complete water evaporation and the formation of a gel and subsequently a solid resin. The beaker was then removed from the hot plate and placed in a furnace preheated at T ~ 550 °C in air overnight to remove nitrate and carbonate residues. The precursor was then ground and pressed into pellets (2 mm thickness, 13 mm diameter) which were annealed in a tube furnace under 5% H_2/N_2 flow at 800 °C and then at 750 °C for 12 h with intermediate grinding and pelleting. The final cooling rate was at 2 °C min^{-1}.

Phase purity was assessed from powder X-ray diffraction (XRD) patterns collected at room temperature over the range $10 \leq 2\theta \leq 120°$, $\Delta 2\theta = 0.02°$ using a Bruker AXS D8 Advance diffractometer in Bragg-Brentano geometry, and equipped with Ge (1 1 1) Johansson-Guinier focusing primary monochromator

(Cu-Kα_1 radiation) and a silicon strip Lynxeye detector. Thermogravimetric analysis (TGA) was carried out with a Netzsch STA 449 F3 instrument. Samples weighing ~ 100 mg were loaded into platinum crucibles and heated/cooled at a rate of 5 °C min^{-1} in 1 atm. of dry air (flow rate 40 mL min^{-1}) or 5% H_2/N_2 (flow rate 20 mL min^{-1}).

The crystal structure of the samples was further probed by means of transmission electron microscopy (TEM) using a JEOL2100 LaB_6 instrument operating at 200 kV. The samples were crushed in dry ethanol and a drop of the suspension was deposited on a carbon-coated film (copper grid). Diffraction patterns were collected with a GATAN Orius 200D Charge Coupled Device (CCD) camera.

In situ neutron powder diffraction data were collected on the high-flux medium resolution POLARIS diffractometer at ISIS, the UK spallation source at the Rutherford Appleton Laboratory. Approximately 4 g of $NdBaMn_2O_{5+\delta}$ powder were loaded to a depth of 4cm (corresponding to the height of the incident neutron beam) in a double-walled quartz glass cell built to enable gas to flow through the sample in the neutron beam. The cell was mounted in a furnace designed for neutron diffraction measurements and connected to an external gas-handling system, allowing the composition of the gas stream (*e.g.* 5% H_2/He; dry air; water vapour) to be changed as required. Four heating/cooling protocols up to a maximum temperature of 800 °C were applied sequentially, according to the temperature profile illustrated in Figure 1.

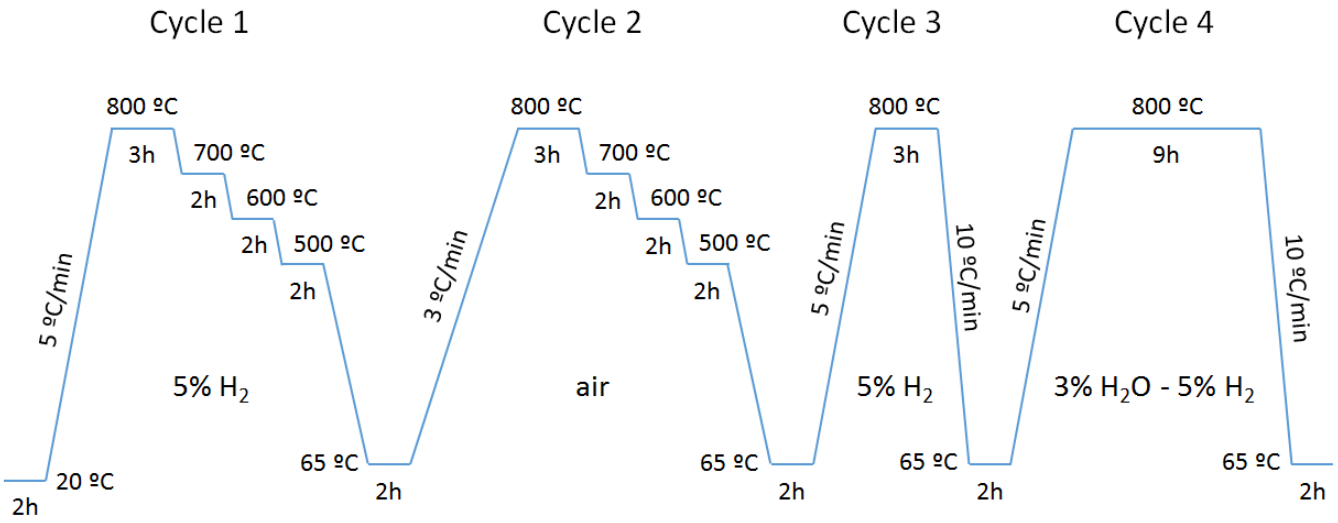

Figure 1. Sequential thermal profiles used in the neutron diffraction experiment of $NdBaMn_2O_{5+\delta}$. In cycles 1 and 2, a cooling rate of 5 °C min^{-1} has been used.

The humid atmosphere in cycle 4 was generated with H_2O-saturated 5% H_2/He (pH_2O ~ 0.030 atm). Two thermocouples were attached on opposite sides of the wall of the (inner) quartz tube approx. 5mm above the sample to control the furnace temperature and monitor the sample temperature. Data normalization and file output was undertaken using the Mantid software package[13]. The patterns from two banks of detectors; the backscattering bank (average 2θ = 146.7°) which covers a range in 2θ from 135 to 167° with a *d*-spacing range of 0.2-2.65 Å and the 90° bank (average 2θ = 92.6°) which covers a 2θ range of 75 to 113° with a maximum *d*-spacing of 4.1 Å were used together for structure refinement by the Rietveld method, using the FullProf Suite program[14]. Peak shapes were modeled by a convolution of two back-to-back exponentials with a pseudo-Voigt function. The background arising from the amorphous quartz glass cell was fitted by the Fourier filtering technique. In addition to the profile parameter (σ_1) describing the Gaussian contribution to the Bragg peak profiles, lattice parameters, fractional occupancy of oxygen sites, atomic positions and atomic displacement parameters (either isotropic or anisotropic) were refined. Any additional constraints are noted when describing specific models. Neutron diffraction results are presented in four parts corresponding to the heating/cooling cycles depicted in Fig. 1.

3. Results and discussion

3.1 Synthesis

The *A*-site ordered $NdBaMn_2O_{5+\delta}$ (δ ~ 0) phase has previously been prepared by sol-gel or solid state reaction methods[12, 15, 16]. This double perovskite is difficult to prepare in a pure form and controlled oxygen atmosphere and temperature are required. Our single step process consists of annealing the precursors under 5% H_2/N_2 at 800 °C and 750 °C for two periods of 12 h with an intermediate regrind and preparation of new pellets between these two annealing periods. Our synthesis method also differs

from the two-step process used to obtain $PrBaMn_2O_{5+\delta}$[10] and from the synthesis under argon atmosphere at T ~ 1350 °C[15] or under 1% H_2/Ar atmosphere at 1100 °C[16] previously used to prepare the $Ln BaMn_2O_{5+\delta}$ (*Ln* = La, Pr, Nd, Sm, Gd, Y) compounds. A reducing atmosphere ($pO_2 < 10^{-4}$ atm) is necessary to avoid the formation of the *A*-site disordered $Nd_{0.5}Ba_{0.5}MnO_3$ perovskite[10] and hexagonal perovskite impurities such as $BaMnO_{3-\delta}$[6, 17].

Thermogravimetric analysis (TGA) of a small part of the as-prepared $NdBaMn_2O_5$ sample was carried out under flowing air and showed that oxidation to $NdBaMn_2O_6$ occurs in a single step on heating, at T ~ 200 °C (Fig. S1) with a weight gain corresponding to 6 oxygen atoms per formula unit (f.u.). A subsequent TGA cycle carried out under 5% H_2/N_2 showed that the phase change from $NdBaMn_2O_6$ to $NdBaMn_2O_5$, hereafter referred to as "O_6" and "O_5" respectively, proceeds between T ~ 400 and 800 °C. No clear indication of any transient phase is observed on the TGA curve under air or under hydrogen with the heating/cooling rates of 5 °C min^{-1} used.

On the basis of these TGA results a sample of fully oxidised *A*-site ordered $NdBaMn_2O_6$ was prepared for X-ray diffraction by taking a fraction of the as-prepared $NdBaMn_2O_5$ sample and heating it under dry air flow at T ~ 800 °C for 36 h.

3.2 Crystal structure of $NdBaMn_2O_{5+\delta}$ and $NdBaMn_2O_{6+\delta}$ at room temperature from X-ray powder diffraction

Although the $a_p \times 2a_p \times 2a_p$ *P4/mmm* and $\sqrt{2}a_p \times \sqrt{2}a_p \times 2a_p$ *P4/nmm* models (a_p refers to the cubic perovskite structure) gave equivalent fits to the X-ray diffraction (XRD) data of $NdBaMn_2O_{5+\delta}$, the latter was chosen on the basis of electron and neutron diffraction studies. The diffraction profile of $NdBaMn_2O_{5+\delta}$, displayed in Fig. S2, gave lattice parameters a = 5.61512(2) Å and c = 7.73895(4) Å, consistent with the values reported for the compound prepared by solid-state reaction[16, 18]. The structure, illustrated in Figure 2, is similar to that of $YBaCuFeO_5$[19] and consists of two distinct square pyramidal Mn sites accounting for Mn^{2+}/Mn^{3+} charge ordering. Oxygen vacancies are located in the lanthanide layers.

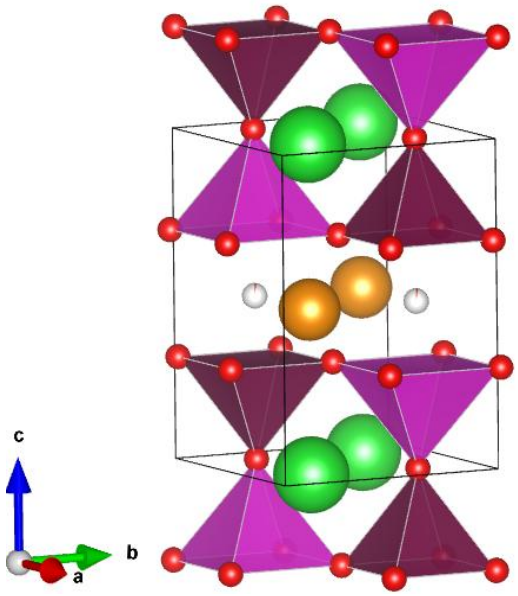

Figure 2. Schematic crystal structure of $NdBaMn_2O_5$ (S.G. *P*4/*nmm*) with (burgundy) $Mn^{3+}O_5$ and (purple) $Mn^{2+}O_5$ forming double pyramidal layers containing (green) Ba^{2+} cations and interleaved with (gold) Nd^{3+} layers**.**

The XRD pattern obtained at room temperature of the "O_6" compound, Fig. S2, shows the (220) reflection of the tetragonal "O_5" unit cell has split into 2 peaks at $2\theta \sim 46.5°$, indicating a lowering of symmetry to orthorhombic. The crystal structure of this fully oxidized phase has an $a_p \times a_p \times 2a_p$ *Pmmm* cell with a = 3.90331(2), b = 3.89244(3) and c = 7.72923(4) Å. Previous studies assigned the structure of $NdBaMn_2O_6$ to be tetragonal (S.G. *P*4/*mmm*)[12, 15] with a = 3.8987(3) and c = 7.7278(7) Å or triclinic (*S.G. P*-1)[16] with a = 5.5177(1), b = 5.5167(1), c = 7.7282(1) Å, $\alpha, \beta \sim 90°$ and $\gamma \sim 90.1°$. Upon oxidation, the normalised lattice parameters (*i.e.* divided to obtain cubic like $a_p \times a_p \times c_p$ unit cell) decrease; $a_p(O_{5.0}) \sim 3.97$ Å, $c_p(O_{5.0}) \sim 3.87$ Å and $V(O_{5.0}) \sim 61.0$ Å^3 *versus* $a_p(O_{6.0}) \sim 3.90$ Å, $c_p(O_{6.0}) \sim 3.86$ Å and $V(O_{6.0}) \sim 58.7$ Å^3 resulting in significant volume contraction, $\Delta V/V \sim -3.7$ % which could be considered as an issue for the application, particularly during the first cell utilisation. However, such a value is much lower than the volume contraction of NiO reducing to Ni, $\Delta V/V \sim -40\%$ in the conventional Ni-based cermet anodes, a problem to which technical solutions have been found [20] and references therein.

3.3 Electron diffraction of $NdBaMn_2O_5$

Figure 3 presents selected area electron diffraction (SAED) patterns obtained after successive rotations of a crystal along the [1-10]* direction of the pseudo-cubic cell. They indicate the doubling of unit cell along *c* (Fig.3a) and weak superstructure reflections that could be indexed in a $\sqrt{2}a_p \times \sqrt{2}a_p \times 2a_p$ supercell. The reflection 1 -1 0, 3 -3 0 etc. are present in Figs. 3a and 3b but absent in Fig. 3c as indicated by arrows at their expected positions. Such observation suggests that these reflections result from multiple scattering and are forbidden in the crystal space group. Consequently, the *P*4/*nmm* space group is considered.

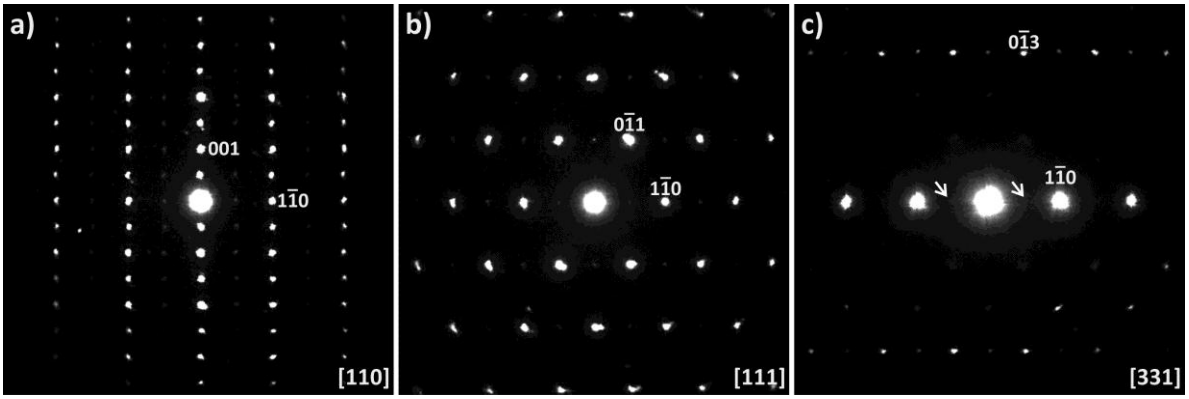

Figure 3. SAED patterns of $NdBaMn_2O_5$ indexed in an $a_p \times a_p \times a_p$ perovskite cubic cell with view along a) [110], b) [111] and c) [331] zone axes.

3.4 Neutron diffraction study

3.4.1 Cycle 1 under 5% H_2/He

The observed, calculated, and difference profiles for the sample at *RT* are displayed in Figure 4. The neutron diffraction profile recorded from the "O_5" sample is perfectly fitted with the tetragonal *P*4/*nmm* model yielding $a \sim 5.6140(1)$ and $c \sim 7.7430(2)$ Å. An impurity was identified as MnO and its amount represented less than 1 wt. % of the sample mass. A MnO impurity usually forms in the synthesis of the *Ln*$BaMn_2O_5$ compounds (*Ln* = Y or rare earth) as observed in $LaBaMn_2O_5$[21]. The *P*4/*nmm* model

accounting for the rocksalt-type charge ordered description was confirmed by the presence of low intensity peaks, e.g. (302) at d ~ 1.68 Å and (301) at d ~ 1.82 Å, highlighted in Fig. 4. The oxygen occupation at the O2 site (in the Ba layer) and O3 site (in the Mn layers) was fixed at 1 since no significant deviation from unity was found through the Rietveld model refinement. The thermal vibration parameters of all the atoms were refined isotropically and were constrained to be equal for O1 and O2 because of the low occupancy at the O1 site. The refined occupancy at the O1 site converged to 0.02(1) giving the composition $NdBaMn_2O_{5.02(1)}$. The presence of oxygen vacancies solely in the Nd layer is induced by Nd/Ba cation ordering. The structural parameters and agreement factors are listed in Table 1.

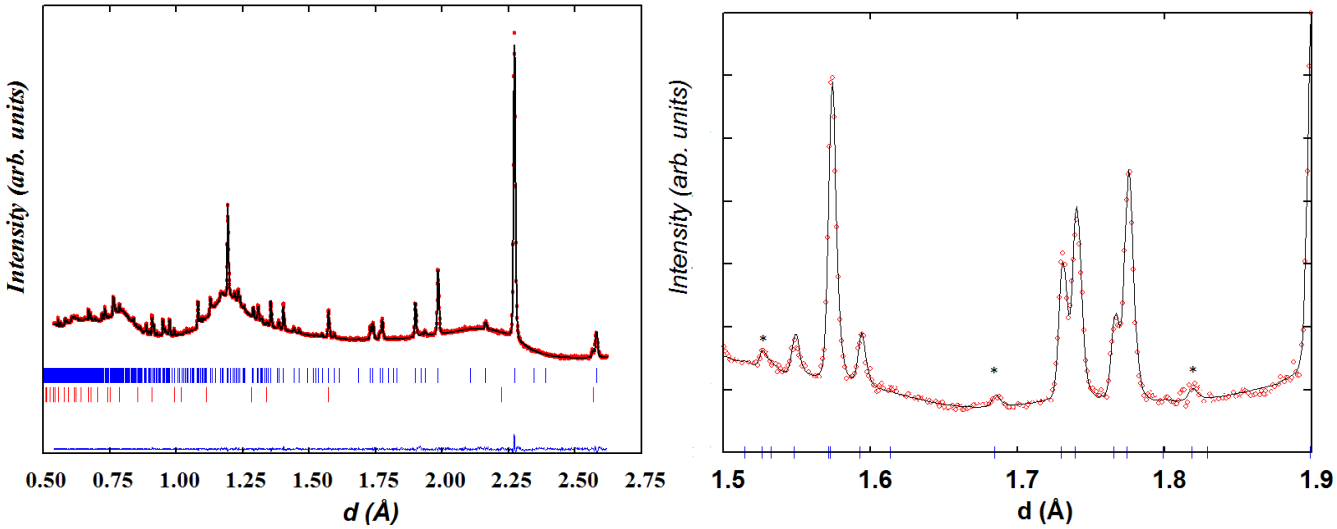

Figure 4. Rietveld refinement plot of the neutron diffraction data (backscattering bank) recorded at *RT* of $NdBaMn_2O_5$ indexed in *P*4/*nmm* (upper markers) and MnO impurity <1 wt. % (lower markers) indexed in *Fd*-3*m*. Figure at the right side highlights superstructure peaks (*) originating from Mn^{2+}/Mn^{3+} charge ordering.

Table 1. Refined lattice parameters, site occupancies and isotropic thermal vibration parameters B_{iso}(Å^2) at 25 °C for as-prepared $NdBaMn_2O_5$ in space group *P*4/*nmm* with atoms in the following positions: Nd, 2b (3/4, 1/4, 1/2); Ba, 2a (3/4, 1/4, 0); Mn1(Mn^{2+}), 2*c* (1/4, 1/4, z); Mn2(Mn^{3+}), 2*c* (1/4, 1/4, z);O1, 2*c* (1/4, 1/4, 1/2); O2, 2c (1/4, 1/4, z); O3, 8*j* (*x*, *x*, *z*).

Atom		
	a (Å)	5.6140(1)
	c (Å)	7.7430(2)
Nd	B_{iso}	0.38(1)
Ba	B_{iso}	0.59(3)
Mn1	*z*	0.2685(5)
	B_{iso}	0.19(6)
Mn2	*z*	0.7495(6)
	B_{iso}	0.31(7)
O1	occ	0.02(1)
	B_{iso}	0.82(2)
O2	*z*	0.0075(6)
	B_{iso}	0.82(2)
O3	*x*	0.4921(2
	z	0.30794(8)
	B_{iso}	0.72(1)
	χ^2	1.56
	R_B %	2.21

*B_{iso} for the O1 and O2 sites were constrained to be equal, the occupation for O2 and O3 was fixed at 1.

The sample was heated at 5 °C min^{-1} and when the temperature had reached 800 °C, isothermal data were collected for 3 hours. The *P*4/*mmm* and *P*4/*nmm* models gave equivalent fits to the neutron data (χ^2 ~ 2.0) meaning that the rock-salt charge ordered arrangement in $NdBaMn_2O_5$ was lost. The observed, calculated and difference profiles recorded at 800 °C are displayed in Figure 5 and the structural parameters and agreement factors are listed in Table 2.

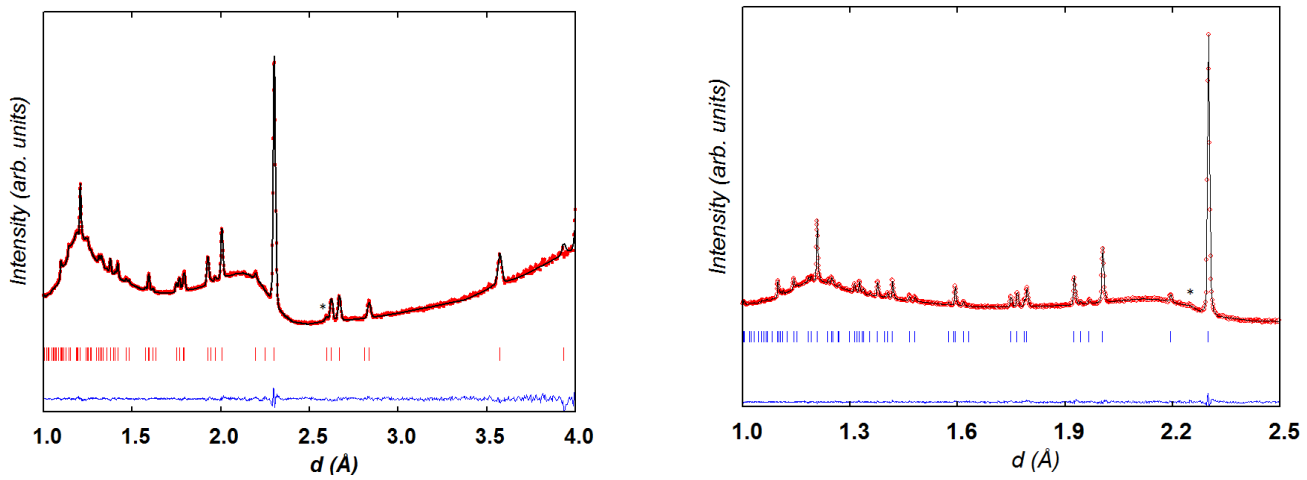

Figure 5. Neutron powder diffraction profiles for the sample $NdBaMn_2O_5$ 800 °C under 5% H_2/He; S.G. *P*4/*mmm*, χ^2 ~ 2.23, (left) fitted 2θ ~ 90° bank data, (right) fitted backscattering profile. The asterisks relate to peaks from MnO impurity.

Table 2. Refined lattice parameters, site occupancies and isotropic thermal vibration parameters B_{iso}(Å^2) for $NdBaMn_2O_5$ at 800 °C (cycle 1) in space group *P*4/*mmm* with atoms in the following positions: Nd, 1*a* (0, 0, 0); Ba, 1*b* (0, 0, 1/2); Mn, 2*h* (1/2, 1/2, z); O1, 1*c* (1/2, 1/2, 0); O2, 1*d* (1/2, 1/2, 1/2); O3, 4*i* (1/2, 0, *z*). B_{iso} for O1 and O2 were constrained to be equal.

Atom		
	a (Å)	4.0108(1)
	c (Å)	7.8706(3)
Nd	B_{iso}	1.56(3)
Ba	B_{iso}	2.51(7)
Mn	*z*	0.2419(4)
	B_{iso}	1.89(5)
O1	occ	0.032(8)
	B_{iso}	2.83(6)
O2	B_{iso}	2.83(6)
O3	*Z*	0.1919(2)
	B_{iso}	2.97(3)
	χ^2	2.23
	R_B%	4.3

The charges at the two Mn sites, estimated from the measured bond distances using the bond valence sum (BVS) method[22], reveal substantial Mn^{2+}/Mn^{3+} charge ordering (CO) at 25 °C (Table 3) with the degree of charge separation estimated at ~ 56% of the theoretical separation of 1 charge unit. Moreover, the refined distances suggest dz^2 orbital ordering in the $Mn^{3+}O_5$ square pyramids. The degree of CO in oxides is always reduced from the ideal value, typically to 20-80% of the ideal separation[23], so the value for $NdBaMn_2O_5$ is in the middle of this range. The estimated BVS sums calculated for the data recorded at 800 °C for the Mn1 and Mn2 sites assuming the *P*4/*nmm* model are within +/-2.5 standard deviations (Table 3) indicating loss of the charge ordering consistent with similar mean Mn-O distances within the two MnO_5 polyhedra. The isothermal data collected for 2 h at 600 and 500 °C on cooling at a rate of 5 °C min^{-1} shows a slightly improved fit with the *P*4/*nmm* model in comparison to the *P*4/*mmm* model. This agrees with the BVS' for the two Mn sites with charge separation of ~ 20% at 600 °C and ~ 35% at 500 °C (Table 3). It is worth emphasising that CO occurs at much higher temperatures in double perovskite manganites (*e.g.* $TbBaMn_2O_5$, T_{CO} > 873 K)[24] than in ferrite and cobaltite structural analogues (*e.g.*, $TbBaFe_2O_5$, T_{CO} ~ 282 K[25], $YBaCo_2O_5$, T_{CO} ~ 220 K [26]) and the disordered perovskite manganites (*e.g.* $Sm_{0.5}Ca_{0.5}MnO_3$, T_{CO} ~ 270 K[27] and $Pr_{0.5}Ca_{0.5}MnO_3$, T_{CO} ~ 140 K[28]).

Table 3. Temperature variation of the Mn-O distances (Å), Mn valence (V) [a] and degree of charge order (%CO) [b] in $NdBaMn_2O_5$ (S.G *P*4/*nmm*) in cycle 1.

Bond/Temperature	25 °C	800 °C	700 °C	600 °C	500 °C
1 × Mn1-O2	2.023(6)	2.04(2)	2.06(2)	2.00(1)	2.05(1)
4 × Mn1-O3	1.947(1)	2.03(1)	2.02(1)	2.007(6)	1.984(5)
<Mn1-O>	1.962(1)	2.035(1)	2.028(5)	2.007(4)	1.997(3)
V_1	2.91(1)	2.38	2.43(3)	2.57(2)	2.64(2)
1 × Mn2-O2	1.997(7)	2.02(2)	2.01(2)	2.05(1)	2.01(1)
4 × Mn2-O3	2.095(2)	2.06(1)	2.06(1)	2.07(7)	2.084(5)
<Mn2-O>	2.075(1)	2.05(1)	2.053(5)	2.065(4)	2.070(3)
V_2	2.33(1)	2.49(4)	2.46(4)	2.38(3)	2.35(2)
%CO	56	0	0	20	35

[a] the BVS calculated as $V_n = \sum \exp(d_n - d_i)/B$ using the parameters reported by Brese *et al*[29] d_i is the bond distances from each metal site to the coordinating oxygens; *B* is a global constant equal to 0.37 in the present case and d_n is the bond valence parameter for the metal in an assumed oxidation state *n*.
[b] $\%CO = 100\ (V_2-V_1)\ (F_H+F_L)/(V_2+V_1)\ (F_H-F_L)$ where V_1 and V_2 are the lower and higher bond valence sums calculated from experimental bond distances and *F*'s are the formal valences in the higher (*H*) and lower (*L*) states, e.g., $F_L = 2$, $F_H = 3$ in $NdBaMn_2O_5$.

Figure 6 shows the temperature dependence of the normalized *a* and *c* lattice parameters on cooling under hydrogen. The slight deviation from linearity observed below *T* ~ 500 °C for the *a* lattice parameter may be associated with the charge disorder/order phase transition. The average thermal expansion coefficient TEC ~ 15 $\times 10^{-6}$ K^{-1}, calculated over the temperature range 65-800 °C, is in relatively good agreement with the data reported recently[9,13] and compatible with TEC values of ceria electrolytes (TEC ~ 12–13 $\times 10^{-6}$ K^{-1} for GDC[30] rather than 8YSZ (TEC ~$10^{-11} \times 10^{-6}$ K^{-1})[31] or LSGM (TEC ~ 11-12 $\times 10^{-6}$ K^{-1}) [32].

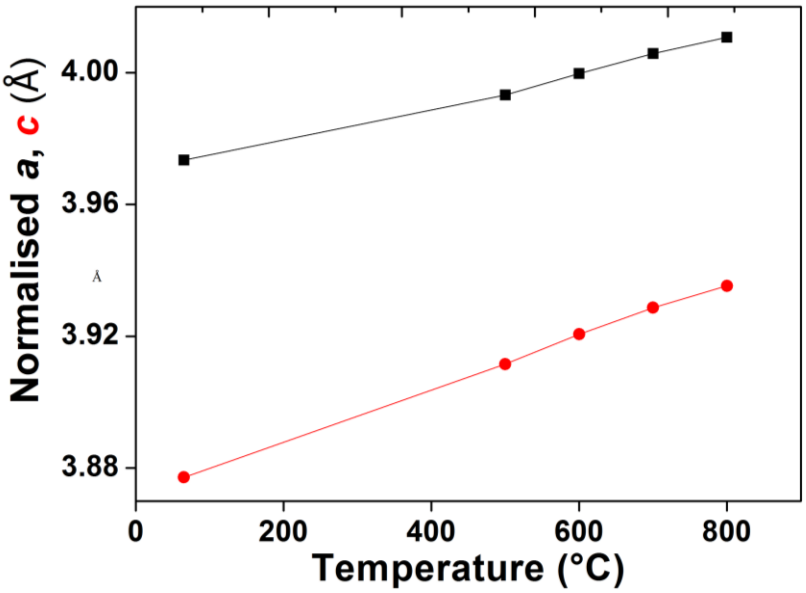

Figure 6. Evolution of the normalized *a* and *c* lattice parameters of $NdBaMn_2O_5$ on cooling in 5% H_2/He flow.

The neutron diffraction data collected under 5% H_2/He at 65 °C for 2h after cooling shows additional small intensity reflections at the high *d* side of the main peaks. These peaks were observed to a lesser extent at 500 °C on cooling (Fig. 7).

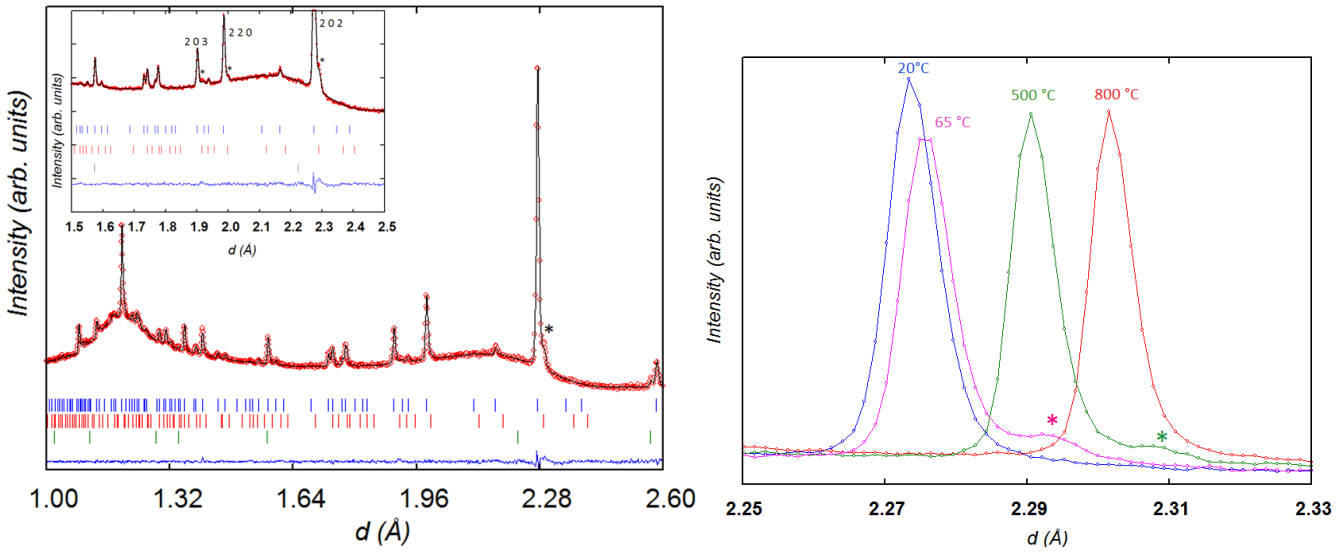

Figure 7. Neutron powder diffraction profile at 65 °C after cycle 1 of the sample consisting of $NdBaMn_2O_5$ (upper markers), the new phase (middle markers) and MnO (lower markers) with insight highlighting a few peaks (*) of the new phase. (Right) evolution of the (202) peak of $NdBaMn_2O_5$ and main peak (*) originating from the new phase on cooling.

These reflections can be indexed in a slightly larger tetragonal ($a_p \times a_p \times 2a_p$) *P*4/*mmm* cell ($a_p$ = 3.992(1) and c_p = 3.912(3) Å) than the main *P*4/*nmm* one (a_p= 3.973(1) and c_p = 3.877(2) Å). The weakness of the extra reflections prevents unambiguous determination of the space group (*e.g..*, *P*4/*nmm versus P*4/*mmm*) and their origin. Assuming the same composition as for the main phase, the contribution of the second phase was estimated at ~ 15 wt. %.

3.4.2 Cycle 2 under air flow

The sample was subsequently heated under air flow on increasing temperature up to 800 °C. On heating a rate of 3 °C min^{-1}, oxygen intercalates in the temperature range 200-355 °C as observed from the growth of the peak attributed to the oxidised phase at *d* ~ 2.25 Å and a decrease of that of the reduced phase at *d* ~ 2.28 Å (Figure 8). As the sample oxidises, the extra peaks observed at the end of cycle 1 whose position is indicated by an asterisk in Fig. 8 vanish progressively.

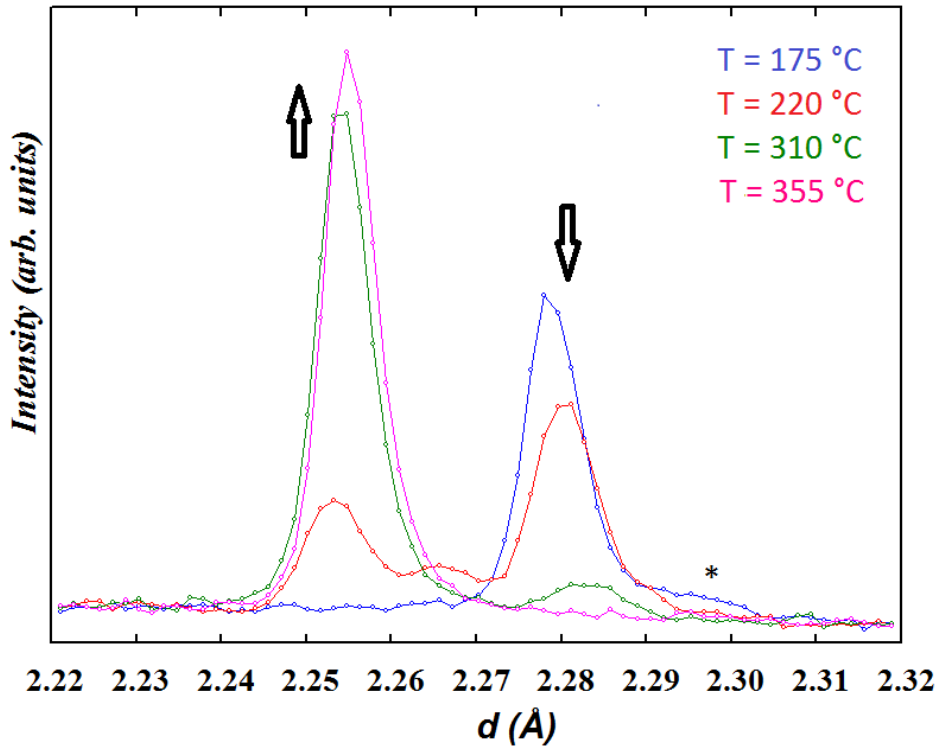

Figure. 8 Selected region of the neutron diffraction patterns collected every 15 minutes on heating $NdBaMn_2O_{5+\delta}$ under flowing. The additional peak (*) that appeared on cooling under hydrogen in cycle 1 disappeared as the oxidation is progressing.

The fitted Rietveld profile of the pattern collected at 800 °C for 3h, displayed in Fig. 9, shows the oxidised phase to be orthorhombic $a_p \times a_p \times 2a_p$ *Pmmm* with lattice parameters a = 3.9325(2), b = 3.9385(2) and c = 7.8323(3) Å. The oxygen content of ~ 5.9(3)/f.u. of this pseudo-tetragonal phase is consistent with full oxidation. The structural parameters are given in Table 4.

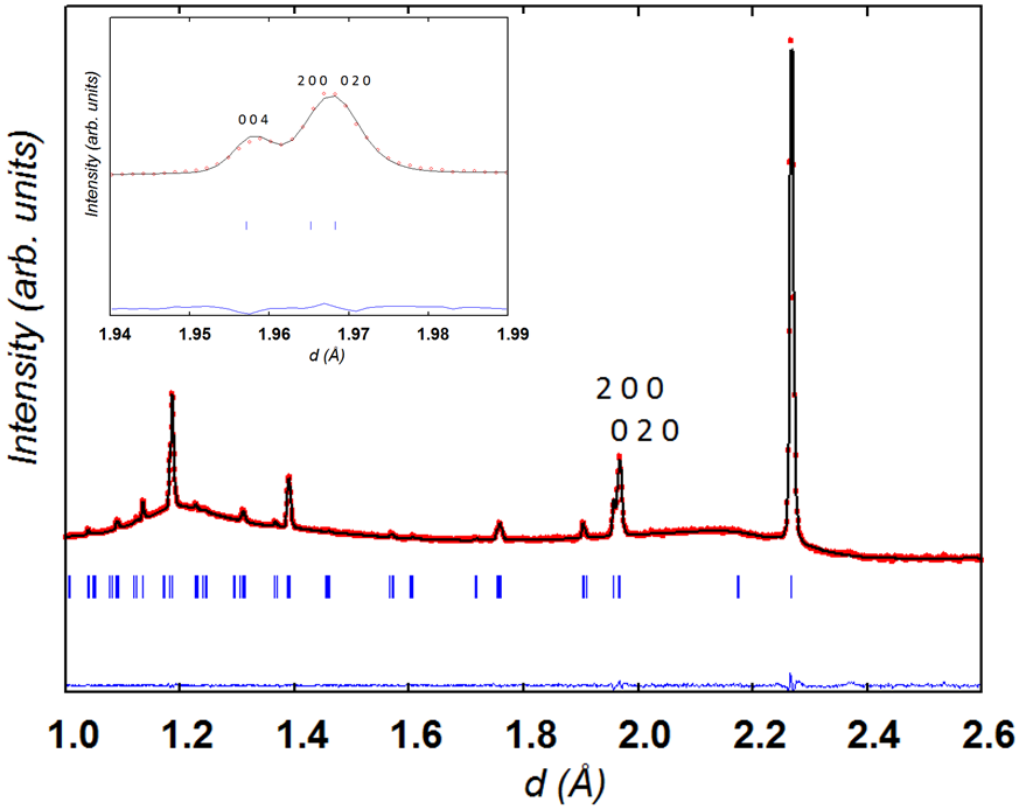

Figure 9. Rietveld refinement (backscattering bank) of $NdBaMn_2O_{5.9(2)}$ in S.G. *Pmmm* at 800 °C under flowing air; data collected for 3 h.

Table 4. Structural results from Rietveld analysis of neutron powder diffraction data for $NdBaMn_2O_{5+\delta}$ at 800 °C under flowing air in space group *Pmmm*.

Atom		
	a (Å)	3.9324(1)
	b (Å)	3.9385(1)
	c (Å)	7.8323(2)
Nd	B_{iso}	1.55(4)
Ba	B_{iso}	1.44(7)
Mn	*z*	0.2485(6)
	B_{iso}	1.20(3)
O1	*occ*	0.96(2)
	B_{iso}	2.8(2)
O2	occ	1.00(2)
	B_{iso}	1.7(1)
O3	*z*	0.226(3)
	occ	1.00(4)
	B_{iso}	2.47(6)
O4	*z*	0.229(3)
	occ	1.00(4)
	B_{iso}	2.47(6)
O-content		5.9(2)
	χ^2	1.78
	R_B %	2.45

On cooling under flowing air, the temperature dependence of the lattice parameters relating to the isothermal data collected for 2h at 700, 600 and 500 °C, is illustrated in Fig. 10. Given the small number of points above 500 degrees and the single point below this temperature, we can assume linear behaviour of the thermal expansion with $\alpha_a \sim 12.57 \times 10^{-6}$ K^{-1}, $\alpha_b \sim 13.84 \times 10^{-6}$ K^{-1} and $\alpha_c \sim 16.77 \times 10^{-6}$ K^{-1} leading to an average TEC value of $\sim 14.40 \times 10^{-6}$ K^{-1}, consistent with those reported earlier (14.3(1) and 14.8(1) $\times 10^{-6}$ K^{-1}) [9,16], confirming good mechanical compatibility of $NdBaMn_2O_{6-\delta}$ with ceria SOFC electrolytes[30].

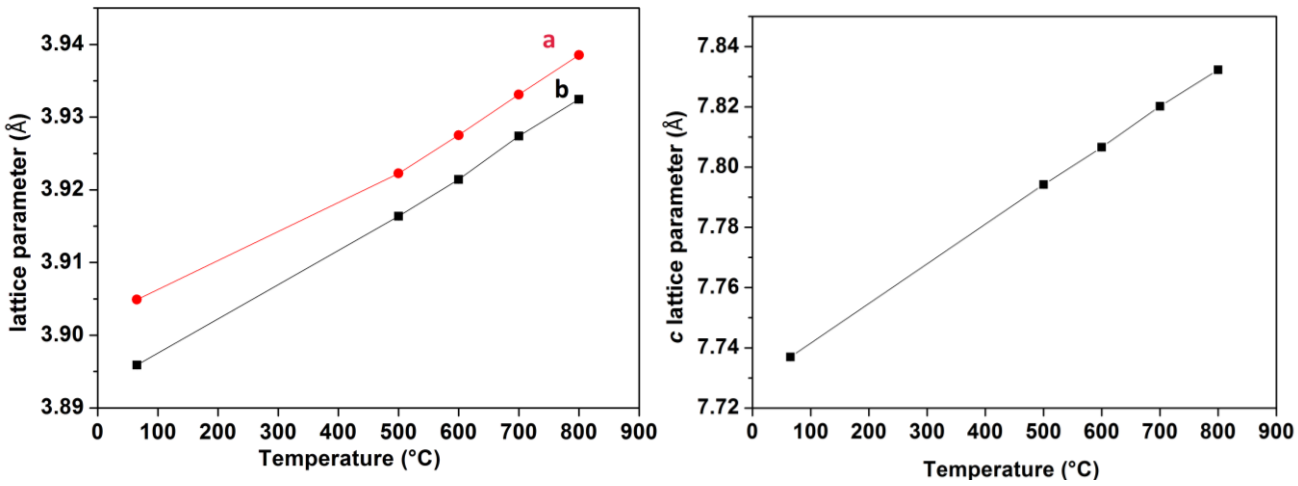

Figure 10. Variation of the lattice parameters of $NdBaMn_2O_{6-\delta}$ (S.G. *Pmmm*) on cooling under air flow. Error bars are smaller than the symbols. $\alpha_a \sim 12.57 \times 10^{-6}$ K^{-1}, $\alpha_b \sim 13.84 \times 10^{-6}$ K^{-1} and $\alpha_c \sim 16.77 \times 10^{-6}$ K^{-1}, $\alpha_V \sim 14.39 \times 10^{-6}$ K^{-1}.

The neutron powder diffraction profile of the oxidised sample recorded at the lowest temperature of 65 °C reached under air is displayed in Figure 11. The lattice parameters and atomic positons are listed in Table 5. The lattice parameters are comparable to those obtained from XRD.

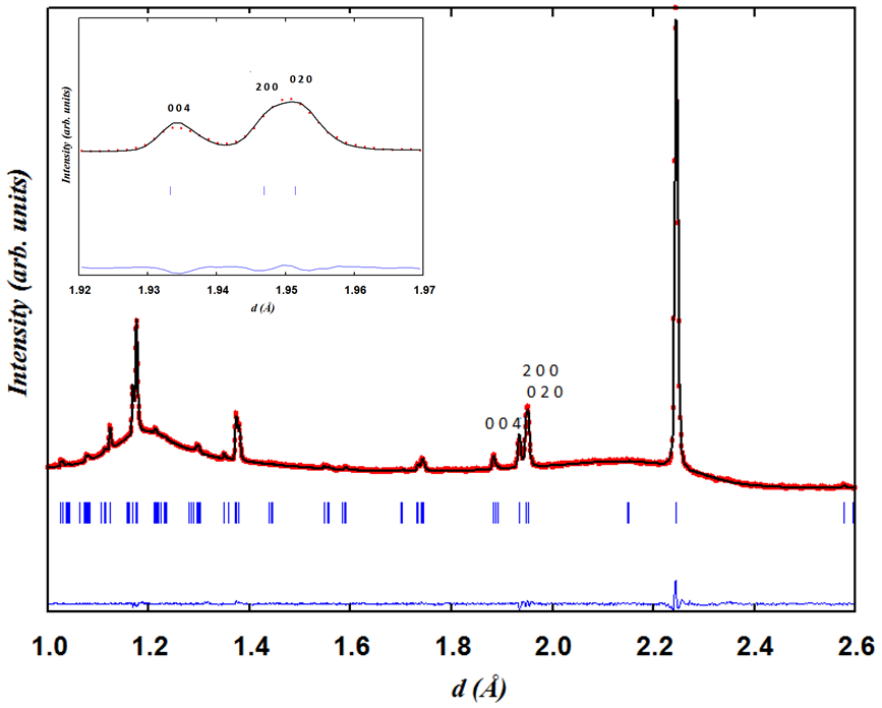

Figure 11. Neutron powder diffraction profile (backscattering bank) of $NdBaMn_2O_{6-\delta}$ (S.G *Pmmm*) collected at 65 °C for 2 h after a heating/cooling cycle under flowing air; the orthorhombic distortion is evidenced by the (200/020) doublet highlighted in the inset.

Table 5. Structural results from Rietveld analysis for $NdBaMn_2O_{6+\delta}$ at 65 °C (end of cycle 2).

Atom		
	a (Å)	3.8958(1)
	b (Å)	3.9048(1)
	c (Å)	7.7370(2)
Nd	B_{iso}	0.68(5)
Ba	B_{iso}	0.29(7)
Mn	*z*	0.2473(4)
	B_{iso}	0.42(2)
O1	*occ*	0.96(2)
	B_{iso}	1.2(1)
O2	occ	0.97(2)
	B_{iso}	0.73(9)
O3	*z*	0.227(2)
	occ	0.99(4)
	B_{iso}	1.1(2)
O4	*z*	0.229(2)
	occ	0.99(4)
	B_{iso}	1.2(2)
O-content		5.9(2)
	χ^2	2.47
	R_B %	2.67

$NdBaMn_2O_{6-\delta}$ displayed no charge order at room temperature in agreement with the finding of Ueda *et al.* in contrast to oxidised samples with smaller Ln^{3+} cations (Sm^{3+} and Gd^{3+})[33].

3.4.3 Cycle 3 under dry 5% H_2 /He

Heating $NdBaMn_2O_{6-\delta}$ under 5% H_2/He promotes oxygen removal with retention of *A*-site ordering. From the diffraction data, the phase change from "O_6 "to the $NdBaMn_2O_{5.5}$ phase, referred as "$O_{5.5}$", is found to occur at T ~ 400 °C whereas the fully reduced "O_5" phase is only detected at T~ 800 °C in our heating conditions (Fig. 12).

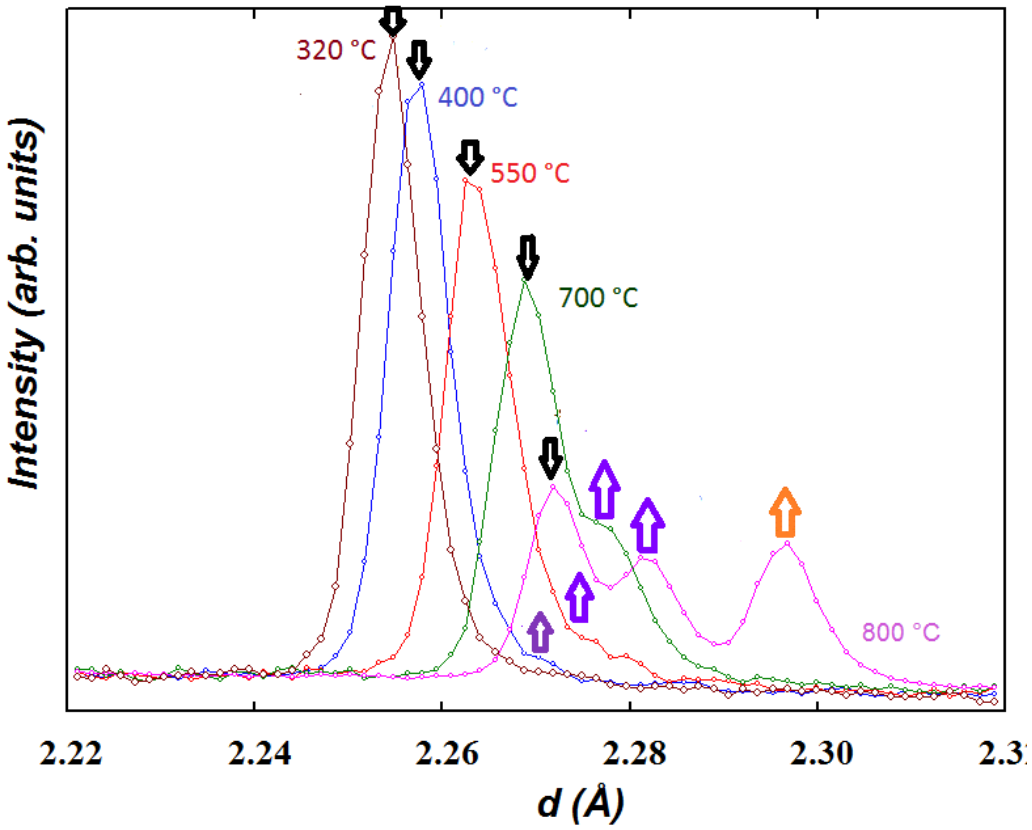

Figure 12. Selected region of the neutron diffraction patterns collected on heating $NdBaMn_2O_{6-\delta}$ under 5% H_2/He (cycle 3), indicated temperatures are average values). The arrows indicate decrease or increase of the different coexisting phases; black: "O_6", purple: "$O_{5.5}$" and yellow: "$O_{5.0}$".

The fraction of the "$O_{5.5}$" phase reaches ~ 25 wt. % at T ~ 700-800 °C (Table 6). The pattern collected for 3h at 800 °C consists of three phases; $NdBaMn_2O_6$ (36 wt. %), $NdBaMn_2O_{5.5}$ (25 wt. %) and $NdBaMn_2O_5$ (39 wt. %). It is interesting to notice that in contrast to slow reduction kinetics, oxidation of the "O_5" phase (section 4.2) was much faster, with the "$O_{6.0}$" phase formed rapidly enough to prevent *in situ* observation of the metastable half-oxygenated "$O_{5.5}$" phase despite the use of a slower heating rate of 3 °C min^{-1} under air *versus* 5 °C min^{-1} under 5% H_2/He.

Table 6. Refined phase fractions of $NdBaMn_2O_6$, $NdBaMn_2O_{5.5}$ and $NdBaMn_2O_5$ (cycle 3).

Temperature (°C)	Wt. % $NdBaMn_2O_6$	Wt. % $NdBaMn_2O_{5.5}$	Wt. % $NdBaMn_2O_5$
320	100	0	0
400	98(1)	2(1)	0
470	96(1)	4(1)	0
550	93(2)	7(2)	0
620	84(2)	16(2)	0
700	73(3)	27(3)	0
800	36(1)	25(1)	39(1)
65	0	31(1)	69(1)

In the multiphase refinement, the $NdBaMn_2O_6$ and $NdBaMn_2O_5$ phases were fitted using the orthorhombic *Pmmm* and tetragonal *P*4/*mmm* models, respectively, as is observed for these phases in cycles 1 and 2. Because of possible correlations between the parameters of related structures, the occupancy-factors at the oxygen sites in $NdBaMn_2O_6$ and $NdBaMn_2O_5$ were fixed at the nominal values since no deviation from the values expected were observed. In addition, the isotropic thermal vibration parameters for the oxygen sites (B_{iso}) were constrained to be equal in each phase. The $NdBaMn_2O_{5.5}$ phase was fitted to an orthorhombic $2a_p \times 2a_p \times 4a_p$ *Icma* model on the basis of the impurity phase detected during the reduction of $NdBaMn_2O_6$ which was assumed to be of the *Icma*-type[16]. The *Icma* structure observed for half-oxygenated layered manganites with small *A*-site cations, such as $YBaMn_2O_{5.5}$[34] and $TbBaMn_2O_{5.5}$[35] consists of alternating pairs of octahedra and pyramids stacked along the *c* direction. In the *ab* plane, chains of pyramids and octahedra alternate along the *a* axis resulting in the presence of tunnels along the *b* axis. A projection of the *Icma* structure for $NdBaMn_2O_{5.5}$ along *b* showing the six different sites for the oxygen atoms is displayed in Figure 13.

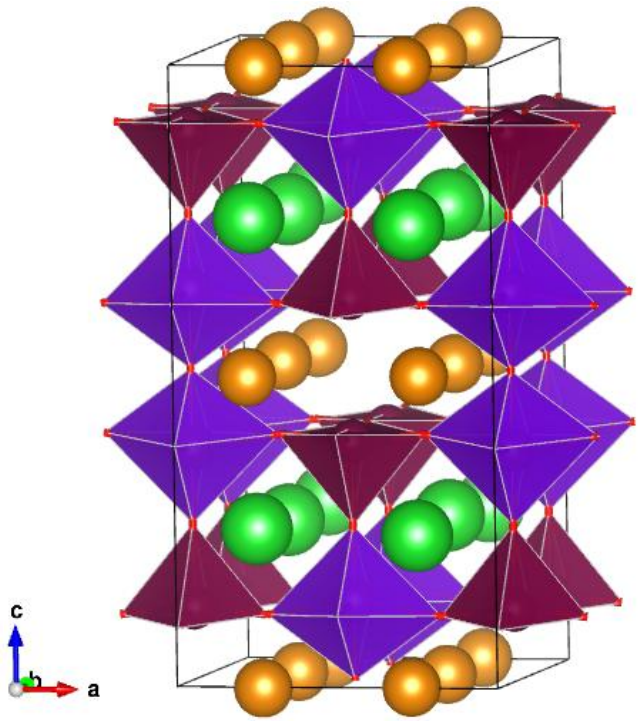

Figure 13. Crystal structure of $NdBaMn_2O_{5.5}$ (S.G. *Icma*); Ba and Nd atoms are represented by green and gold spheres, respectively, Mn1 are in the pyramids and Mn2 in the octahedra, the different sites for the oxygen atoms are indicated.

Fractional occupancies for the oxygen positions were initially refined and the values for O1, O3, O4 (in the Mn layers) and O2 (in the Ba layer) were subsequently fixed at 1 as no significant deviation from unity was found. The site occupancy factors for O5 (in the Nd layer) converged to 1 within +/-1 esds, while the occupancy at the O6 site representing excess oxygen (δ) was negligible and will not be considered for the discussion. Figure 14 shows the neutron profile recorded at 800 °C which consists of $NdBaMn_2O_{5.5+\delta}$ (~25 wt. %), $NdBaMn_2O_5$ (~39 wt. %) and $NdBaMn_2O_6$ (~36 wt. %) and Table 7 lists the structural parameters for $NdBaMn_2O_{5.5+\delta}$ derived from the three-phase refinement. The structural parameters for $NdBaMn_2O_5$ and $NdBaMn_2O_6$ are given in Tables S1 and S2 of the supporting information.

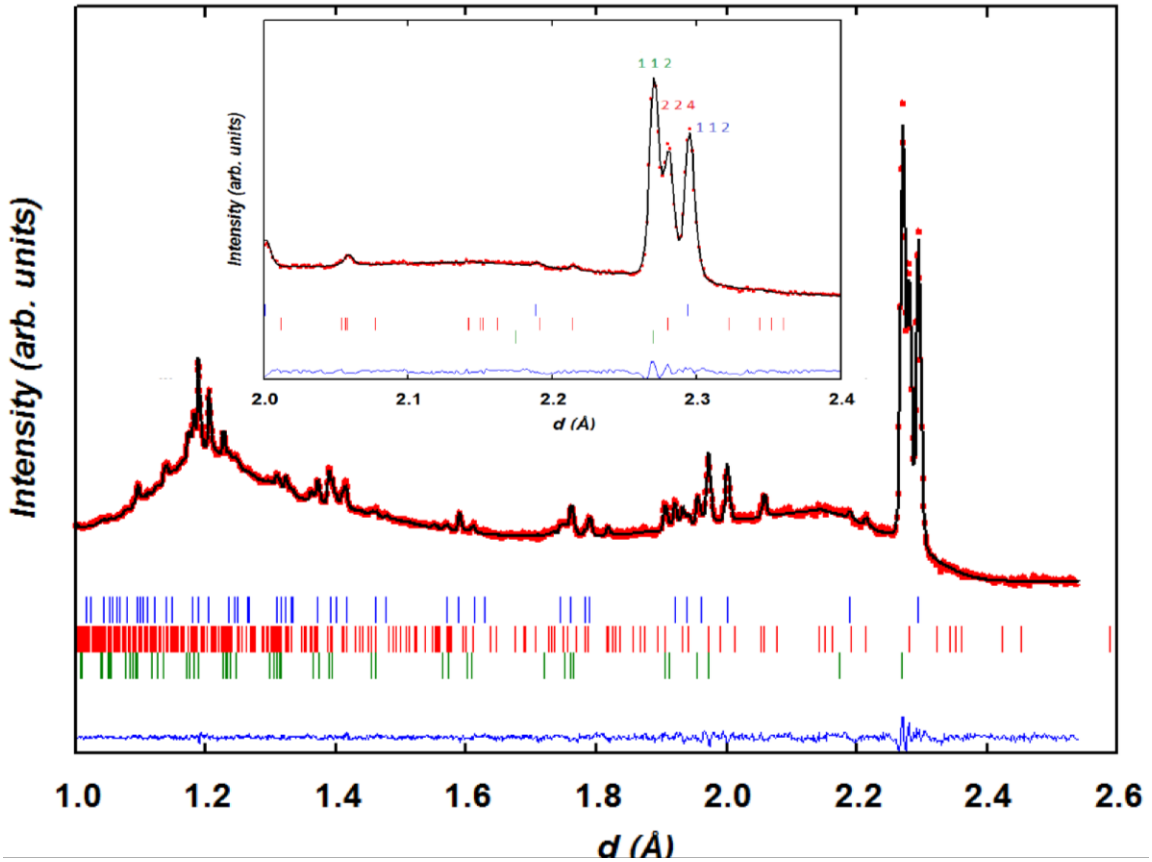

Figure 14. Neutron powder diffraction profile (back scattering bank) of the sample at 800 °C under dry 5% H_2/He (cycle 3) consisting of $NdBaMn_2O_5$ (S.G. *P*4/*mmm*, upper markers) $NdBaMn_2O_{5.5}$ (S.G. *Icma*, middle markers) and $NdBaMn_2O_{6.0}$ (S.G. *Pmmm*, lower markers) The inset highlights the most intense peak in each of the three phases. The contribution of MnO < 1 wt. % has been omitted for clarity.

Table 7. Lattice parameters, coordinates, site occupancies and isotropic thermal vibration parameters B_{iso} (Å^2) for $NdBaMn_2O_{5.5+\delta}$ derived from three-phase refinement at 800 °C (cycle 3) in space group *Icma* with atoms in the following positions: Nd, 8*j* (*x*, 0, *z*); Ba, 8*j* (*x*, 0, *z*); Mn1, 8*f* (0, 1/4, *z*); Mn2, 8*f* (0, 1/4, *z*); O1, 16*k* (*x*, *y*, *z*); O2, 8*f* (0, 1/4, *z*); O3, 8*f* (0, 1/4, *z*); O4, 8*j* (*x*, 0, *z*); O5, 4*b* (0, 1/4, 1/2); O6, 4*a* (0, 1/4, 0), B_{iso} for the oxygen sites were constrained to be equal

Atom		
	a (Å)	8.2353(7)
	b (Å)	7.7320(6)
	c (Å)	15.538(2)
	wt. *%*	25
Nd	*x*	0.262(2)
	z	0.001(3)
	B_{iso}	1.4(2)
Ba	*x*	0.249(3)
	z	0.251(3)
	B_{iso}	0.6(2)
Mn1	*z*	0.116(2)
	B_{iso}	1.0(3)
Mn2	*z*	0.375(2)
	B_{iso}	2.0(5)
O1	*x*	0.223(1)
	y	0.235(2)
	z	0.1044(7)
O2	*z*	0.248(2)
O3	*x*	0.010(5)
	z	0.094(1)
O4	*x*	0.003(6)
	z	0.385(1)
O5	*occ*	0.93(8)
O6	*occ*	0.02(5)
	B_{iso}(O)	2.0(1)
	χ^2	1.1
	R_B %	7.5

It is worth noting that the alternative orthorhombic $a_p \times 2a_p \times 4a_p$ *Ammm* model reported for $LaBaMn_2O_{5.5}$ [36] from a neutron diffraction experiment gave an equivalent fit to the neutron pattern of the $NdBaMn_2O_{5.5}$ phase. The *Ammm* and *Icma* models are closely related, the difference being the antiphase tilting of the Mn polyhedra around the [001] axis in the latter which induces doubling of the lattice parameter *a*. A close examination of the Mn-O-Mn bond angles between neighbouring Mn sites in the *ab* plane (Table 8) reveals that they are larger than in $YBaMn_2O_{5.5}$. The small polyhedral tilting in $NdBaMn_2O_{5.5}$ due to the presence of the larger Nd^{3+} ion compared to Y^{3+} and Tb^{3+} [37] in addition to the high background from the amorphous quartz tube prevents us from detecting extra reflections that

would have allowed unambiguous attribution of *Icma* symmetry on the basis of the neutron diffraction data.

Table 8. Mn-O-Mn bond angles in Å in $NdBaMn_2O_{5.5}$ at 800 °C (cycle 3) in comparison to $YBaMn_2O_{5.5}$ at *RT*[34]

Mn-O-Mn angle	$NdBaMn_2O_{5.5}$	$YBaMn_2O_{5.5}$[34]
Mn1-O1-Mn2	164.8(5)	158.9(1)
Mn1-O3-Mn1	159.1(2)	154.4(5)
Mn2-O4-Mn2	170.6(1)	164.0(3)

The $NdBaMn_2O_{5.5}$ system encompasses the Jahn-Teller Mn^{3+} ion in both 5-coordinate square pyramidal (Mn1) and 6-coordinate octahedral (Mn2) sites as supported by the Bond Valence Sum (BVS) calculations [22] (Table 9) showing small discrepancies from the ideal value of 3. As expected from the emptiness of half of the anion sites in the Nd layer, the 10-coordinated Nd^{3+} cation is underbonded (BVS = 2.56(9) v.u.) and the larger 12-ccordinated Ba^{2+} cation is ideally bonded (BVS = 2.08(6) v.u.). It should however be noticed that the BVS values calculated at 800 °C are underestimated due to thermal expansion.

Table 9. Average interatomic distances and BVS in $NdBaMn_2O_{5.5}$ at 800 °C (cycle3).

Bond	Distance (Å)	Cation BVS (Valence units, v.u.)
<Nd-O>	2.62(1)	2.56(9)
<Ba-O>	2.96(1)	2.08(6)
<Mn1-O>	1.936(8)	3.17(6)
<Mn2-O>	2.068(9)	2.83(8)

A close examination of the interatomic Mn-O distances displayed in Figure 15 reveals cooperative long-range Jahn-Teller distortions of the polyhedra. In the pyramid, the axial Mn1-O2 bond is elongated (2.040 Å) in comparison to the bonds in the *ab* plane, Mn1-O1 (1.849 Å) and Mn-O3 (1.967 Å)

suggesting that the single occupied d_z^2 orbital is along the *c*-axis. Conversely in the octahedron, the Mn2-O1 bonds along the *a*-axis (2.301 Å) are elongated with respect to the Mn-O4 bonds along the *b*-axis (1.939 Å) and the two axial bonds Mn2-O2 (1.972 Å) and Mn2-O5 (1.942 Å), indicating that the d_z^2 orbital is along the *a*-axis.

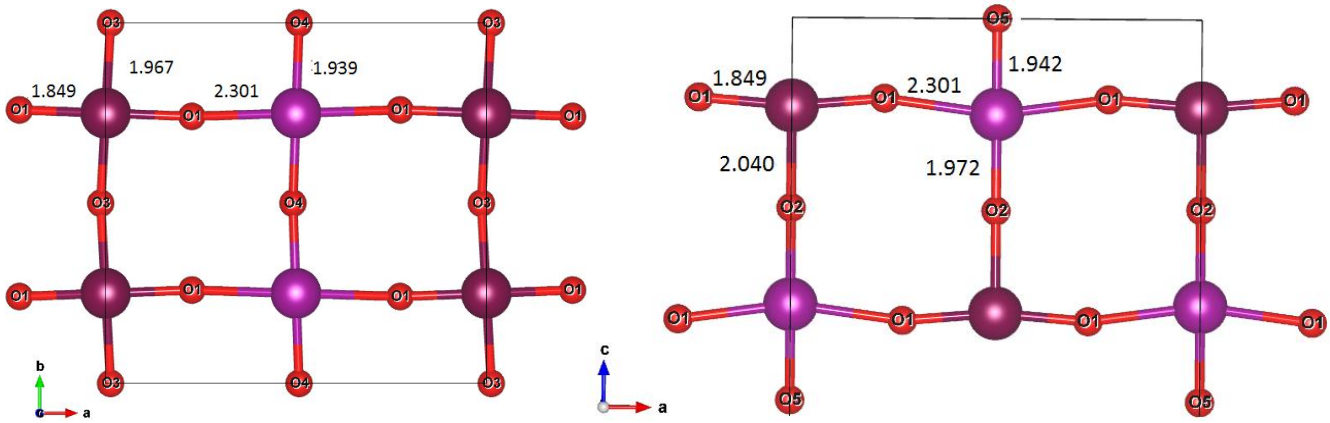

Figure 15. Projection along the [001] and [010] directions for $NdBaMn_2O_{5.5}$ at 800 °C showing the environment of (burgundy) Mn1 in pyramidal coordination and (purple) Mn2 in octahedral coordination. The Mn-O bond lengths in Å are indicated**.**

From these observations, we can confirm that antiferrodistortive orbital ordering is present at 800 °C in $NdBaMn_2O_{5.5}$ as observed for other half-doped manganites at room temperature [34, 36]. Figure 16 illustrates the thermal evolution of the lattice parameters and volume of the "$O_{5.5}$" phase derived from the three phase refinement in cycle 3. The thermal expansion coefficients estimated from the linear fits are $\alpha_a \sim \alpha_b \sim 12.5 \times 10^{-6}\ K^{-1}$ and $\alpha_c \sim 14.0 \times 10^{-6}\ K^{-1}$ resulting in an average TEC value of $\sim 13.0 \times 10^{-6}\ K^{-1}$ compatible with the standard ceria-type SOFC electrolytes [30].

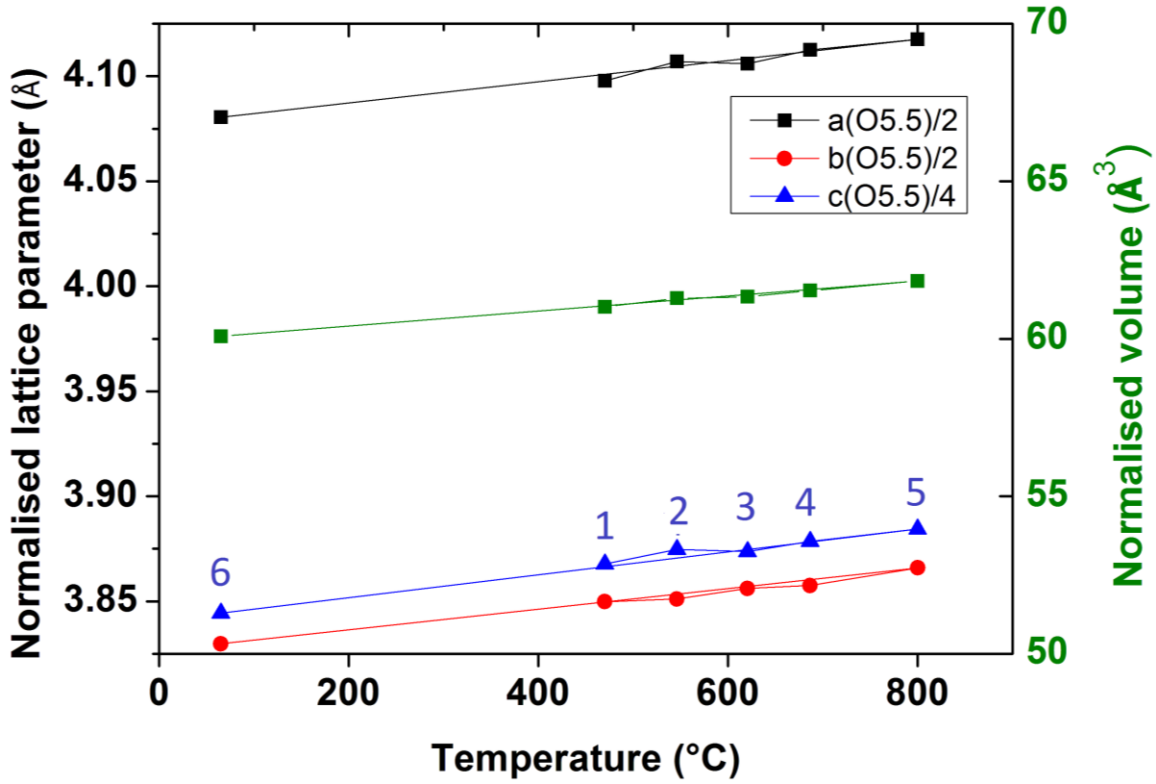

Figure 16. Thermal evolution of the normalised lattice parameters and volume of $NdBaMn_2O_{5.5}$ on heating from *T* ~ 470 °C up to 800 °C and subsequent fast cooling to 65 °C. Heating/ cooling rate are 5 and 10 °C min^{-1}, respectively. Numbers 1-6 indicate the sequence of data collection.

When the temperature has reached 65 °C a cooling isothermal data were collected for 2h. Rietveld refinements reveal that the neutron profile (Figure 17) consisted of the two phases, $NdBaMn_2O_5$ (68 wt. %) and $NdBaMn_2O_{5.5}$ (32 wt. %). The structural parameters of the "$O_{5.5}$" phase are listed in Table 10 and those for the "O_5" compound are given in Table S3 of the supporting information. Despite complete transformation of the "O_6" phase, the presence of a non-negligible amount of the "$O_{5.5}$" phase after more than 7 h cycling under hydrogen highlights slow reduction kinetics of the manganite which would be a drawback for use as an electrode in SOFCs. Slow reduction of $NdBaMn_2O_{6-\delta}$ (several minutes) compared to oxidation (few seconds) has been mentioned by Klimkowicz *et al.*[16], who noticed that despite 220 min heating at 500 °C in 5% H_2/Ar their reduced sample contained ~15 wt. % of *Icma* $NdBaMn_2O_{5.5}$ impurity. Fast oxidation has been explained by its strong exothermicity (with respect to endothermic reduction) causing local overheating of the material speeding up oxygen diffusion in the bulk [38].

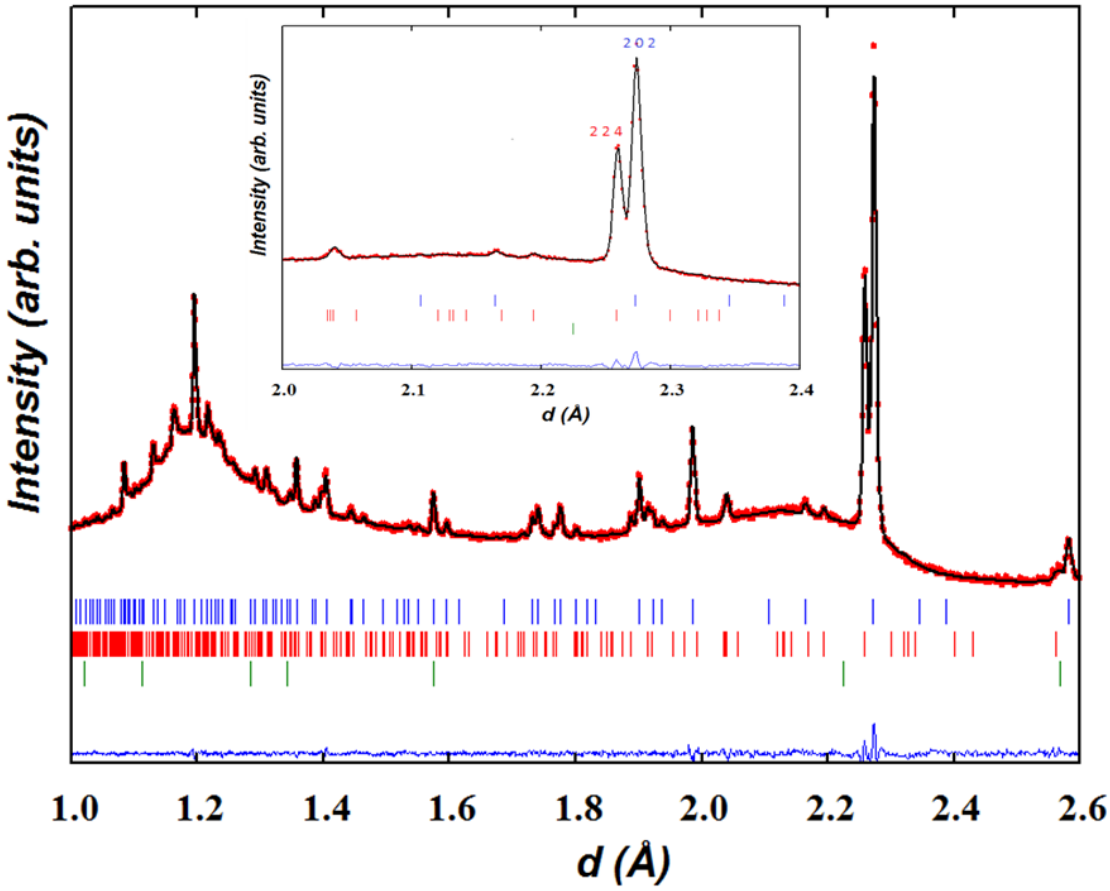

Figure 17. Rietveld refinement plot (back scattering bank) of NPD data at 65 °C after cooling under dry 5% H_2/He (cycle 3); χ^2 ~ 1.3. Bragg peaks indicated by tick marks (top/blue $NdBaMn_2O_5$, ~ 68 wt. %, S.G. *P*4/*nmm*; middle/red $NdBaMn_2O_{5.5}$, ~ 32 wt. %, S.G. *Icma;* bottom/green MnO impurity, < 1wt. %). The inset emphasises the main peak in $NdBaMn_2O_5$ and $NdBaMn_2O_{5.5}$.

Table 10. Lattice parameters, coordinates, site occupancies and isotropic thermal vibration parameters B_{iso} (Å^2) for $NdBaMn_2O_{5.5+\delta}$ (S.G. *Icma*) at 65 °C (cycle 3) derived from two-phase refinement; B_{iso} for the O sites were contained to be equal and the occupancy of the O1-O5 sites was fixed at 1.

Atom		
	a (Å)	8.1610(5)
	b (Å)	7.6596(4)
	c (Å)	15.378(1)
	wt. *%*	32
Nd	*x*	0.267(1)
	z	-0.001(3)
	B_{iso}	0.53(9)
Ba	*x*	0.252(4)
	z	0.251(3)
	B_{iso}	0.56(4)
Mn1	*z*	0.1169(9)
	B_{iso}	0.3(2)
Mn2	*z*	0.3743(9)
	B_{iso}	0.5(2)
O1	*x*	0.2296(9)
	y	0.252(3)
	z	0.1036(4)
O2	*z*	0.2514(7)
O3	*x*	0.015(2)
	z	0.0952(7)
O4	*x*	0.007(3)
	z	0.3858(6)
O6	*occ*	0.08(3)
	B_{iso} (O)	0.63(4)
	χ^2	1.2
	R_B%	4.6

The average Mn-O distances, BVS for the two Mn sites and Mn-O-Mn angles in the *ab* plane at 65 °C, listed in Table 11, show little change with temperature in comparison to 800 °C, as was reported for the related $TbBaMn_2O_{5.5}$ manganite whose structure was studied as a function of temperature up to 600 °C by neutron diffraction [35].

Table 11. Average bond length, BVS and Selected Mn-O-Mn angles in $NdBaMn_2O_{5.5}$ at 65 °C

Bond	Length (Å)	Cation BVS (Valence units, v.u.)	Mn-O-Mn angle	degrees
<Nd-O>	2.640(8)	2.86(8)	Mn1-O1-Mn2	165.0 (3)
<Ba-O>	2.93(1)	2.21(6)	Mn1-O3-Mn1	159.0(1)
<Mn1-O>	1.922(4)	3.13(3)	Mn2-O4-Mn2	168.9(1)
<Mn2-O>	2.023(4)	3.24(4)		

The Mn-O interatomic distances as determined from the data recorded at 65 °C displayed in Figure 18 indicate that orbital ordering between the d_z^2 orbitals of Mn1 (parallel to the *c* axis) and Mn2 (parallel to the *a* axis) is unchanged with respect to $T \sim 800$ °C.

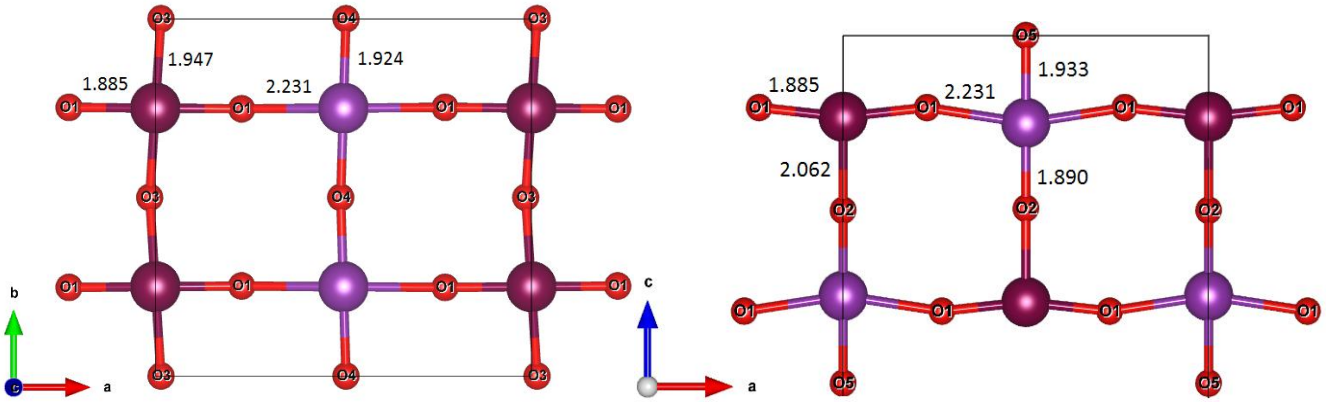

Figure 18. Projection along the [001] and [010] directions for $NdBaMn_2O_{5.5}$ at 65 °C showing the environment of (burgundy) Mn1 in pyramidal coordination and (purple) Mn2 in octahedral coordination. The Mn-O bond lengths in Å are indicated.

3.4.4 Final cycle under wet 5% H_2/He

A subsequent cycle was performed under wet (3% H_2O) dilute hydrogen with a heating/cooling rate of 5 °C min^{-1}. The aim was to complete the reduction and check the stability of the system under wet conditions. As under dry hydrogen (cycle 3) the onset of oxygen loss is detected at $T \sim 400$ °C since the intensity of the peaks originating from the "$O_{5.5}$" and "$O_{5.0}$" phases decreases and increases, respectively with further heating (Fig. 19).

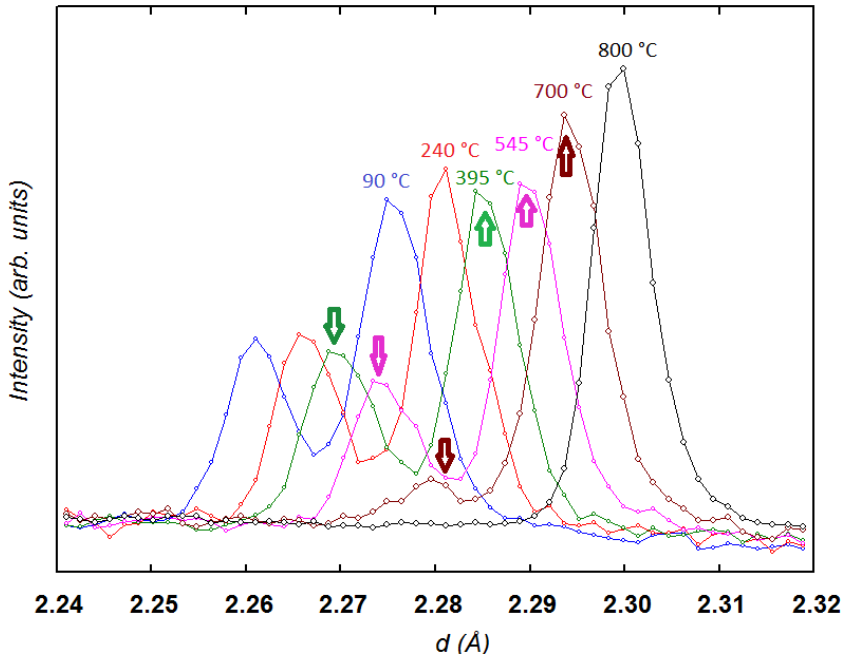

Figure 19. Selected region of the neutron diffraction patterns collected on heating the sample under wet 5% H_2/He in the last cycle (indicated temperatures are average values). The arrows indicate conversion of $NdBaMn_2O_{5.5}$ to $NdBaMn_2O_{5.0}$ proceeding in the temperature range of 395-700 °C. The data set at 800°C consists of the single $NdBaMn_2O_5$ phase.

Figure 20 displays the Rietveld plot of the final pattern collected at 65 °C after all the heating/cooling cycles. Its similarity with the pattern recorded from the "O_5" as-prepared sample in the beginning of the experiment at 25°C in cycle 1 (inset of Fig. 20) confirms clearly the stability of the $NdBaMn_2O_{5+\delta}$ system to redox cycling and to humid conditions up to 800 °C. The additional peaks observed at 65 °C after cooling in cycle 1 are absent at 65 °C in cycle 4 (wet 5% H_2) despite 9 h of heating at 800 °C. Such results suggest that the layered manganite is less prone to "phase transformation" in wet hydrogen than in a dry atmosphere. The structure parameters listed in Table 12 are slightly different from those refined at 25°C for the as-prepared material (cycle 1) due to thermal expansion but the oxygen stoichiometry after the last cycle returned to ~ 5.0.

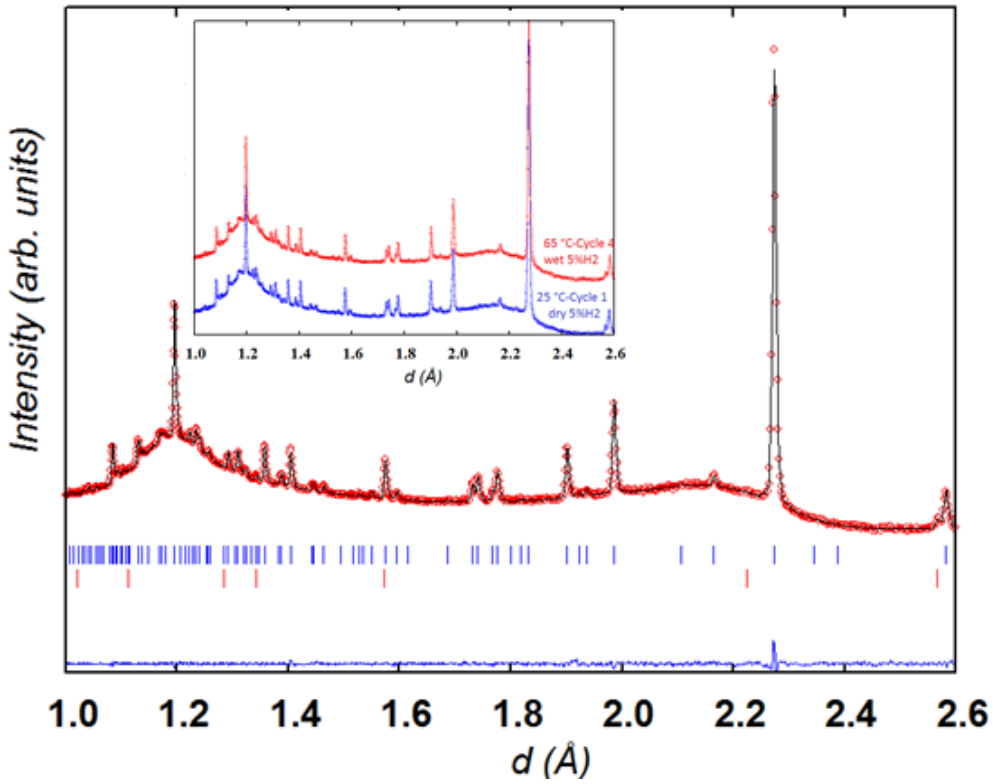

Figure 20. Rietveld refinement for $NdBaMn_2O_{5+\delta}$ (backscattering detector bank) at 65 °C collected for 2h in the end of the neutron experiment after the four heating/cooling cycles. The Bragg peaks are indicated by tick marks (top $NdBaMn_2O_5$ ~ 99 wt. %, S.G. *P*4/*nmm*; bottom MnO, < 1 wt. %, *Fd*-3*m*). The inset compares the patterns of $NdBaMn_2O_5$ at the (blue) beginning and (red) end of the neutron diffraction experiment.

Table 12. Structural parameters for $NdBaMn_2O_{5.0}$ at 65 °C after the last cycle.

Atom		
	a (Å)	5.6164(1)
	c (Å)	7.7509(2)
Nd	B_{iso}	0.42(2)
Ba	B_{iso}	0.72(3)
Mn1	*z*	0.2687(6)
	B_{iso}	0.26(7)
Mn2	*z*	0.7496(6)
	B_{iso}	0.38(7)
O1	occ	0.016(1)
	B_{iso}	0.93(3)
O2	*z*	0.0077(7)
	B_{iso}	0.93(3)
O3	*x*	0.4924(2)
	z	0.30810(9)
	B_{iso}	0.80(1)
	χ^2	1.63
	R_B %	2.36

*B_{iso} for the O1 and O2 sites were constrained to be equal, the occupation for O2 and O3 was fixed at 1.

4. Conclusion

The neutron diffraction experiment allowed monitoring the behavior of the $NdBaMn_2O_{5+\delta}$ SOFC anode candidate material in dilute H_2 gas and air atmospheres over a wide temperature range between 25°C and 800°C relevant to the operating conditions. Three crystalline phases within the $NdBaMn_2O_{5+\delta}$ system with $\delta \sim 0.0, 0.5, 1.0$ were detected and no evidence of oxygen miscibility between them was evidenced up to 800 °C. The capacity of $NdBaMn_2O_{5+\delta}$ for large changes in oxygen content due to rapid oxygen uptake at relatively low temperature contrasts with much slower oxygen release at higher temperature involving the formation of the transient $NdBaMn_2O_{5.5}$ phase. The structural characterisation of this orthorhombic $NdBaMn_2O_{5.5}$ phase as a function of temperature and time under flowing hydrogen evidenced large thermal expansion along with slow anisotropic oxygen diffusion which may be a long-term issue in using $NdBaMn_2O_5$ as anode material despite its high thermal stability to redox cycling and to wet atmosphere, although it is possible that technical solutions can be found, as was done for the Ni-cermet SOFC anodes.

Acknowledgments

The authors thank Chris Goodway, Paul McIntyre and Adam Sears of the ISIS User Support Group for technical assistance with the furnace and gas handling equipment during the neutron diffraction experiment and STFC for provision of neutron beam time. GG and MB thank Mario A. Macias (Universidad Industrial de Santander) and Tamara Mollon (UR1) for their participation in the synthesis of the compound. MB acknowledges T. Roisnel (UR1) for FullProf improvements relating to TOF data analysis. FT thanks the KAUST Academic Excellence Alliance for funding.

References

1. S. C. Singhal, *Solid State Ionics*, 2000, **135**, 305-313.
2. N. Q. Minh, *Solid State Ionics*, 2004, **174**, 271-277.
3. A. Atkinson, S. Barnett, R. J. Gorte, J. T. S. Irvine, A. J. McEvoy, M. Mogensen, S. C. Singhal and J. Vohs, *Nature Materials*, 2004, **3**, 17-27.
4. S. McIntosh and R. J. Gorte, *Chemical Reviews*, 2004, **104**, 4845-4866.
5. M. Bahout, S. S. Pramana, J. M. Hanlon, V. Dorcet, R. I. Smith, S. Paofai and S. J. Skinner, *Journal of Materials Chemistry A*, 2015, **3**, 15420-15431.
6. T. Broux, M. Bahout, J. M. Hanlon, O. Hernandez, S. Paofai, A. Berenov and S. J. Skinner, *Journal of Materials Chemistry A*, 2014, **2**, 17015-17023.
7. Y. Hu, O. Hernandez, T. Broux, M. Bahout, J. Hermet, A. Ottochian, C. Ritter, G. Geneste and G. Dezanneau, *Journal of Materials Chemistry*, 2012, **22**, 18744-18747.
8. A. Klimkowicz, K. Świerczek, K. Zheng, M. Baranowska, A. Takasaki and B. Dabrowski, *Solid State Ionics*, 2014, **262**, 659-663.
9. T. Motohashi, T. Ueda, Y. Masubuchi, M. Takiguchi, T. Setoyama, K. Oshima and S. Kikkawa, *Chemistry of Materials*, 2010, **22**, 3192-3196.
10. S. Sengodan, S. Choi, A. Jun, T. H. Shin, Y.-W. Ju, H. Y. Jeong, J. Shin, J. T. S. Irvine and G. Kim, *Nat Mater*, 2015, **14**, 205-209.
11. T. H. Shin, J.-H. Myung, M. Verbraeken, G. Kim and J. T. S. Irvine, *Faraday Discussions*, 2015, **182**, 227-239.
12. O. L. Pineda, Z. L. Moreno, P. Roussel, K. Świerczek and G. H. Gauthier, *Solid State Ionics*, 2016, DOI: http://dx.doi.org/10.1016/j.ssi.2016.01.022.
13. Mantid, *Manipulation and Analysis Toolkit for Instrument Data. Mantid Project*, 2013.
14. J. Rodríguez-Carvajal, *Physica B: Condensed Matter*, 1993, **192**, 55-69.
15. A. I. Rykov, Y. Ueda and K. Nomura, *Journal of Solid State Chemistry*, 2009, **182**, 2157-2166.
16. A. Klimkowicz, K. Świerczek, A. Takasaki, J. Molenda and B. Dabrowski, *Materials Research Bulletin*, 2015, **65**, 116-122.
17. T. Nakajima, H. Kageyama and Y. Ueda, *Journal of Physics and Chemistry of Solids*, 2002, **63**, 913-916.
18. S. Trukhanov, V. Khomchenko, L. Lobanovski, M. Bushinsky, D. Karpinsky, V. Fedotova, I. Troyanchuk, A. Trukhanov, S. Stepin, R. Szymczak, C. Botez and A. Adair, *Journal of Experimental and Theoretical Physics*, 2006, **103**, 398-410.
19. L. Er-Rakho, C. Michel, P. Lacorre and B. Raveau, *Journal of Solid State Chemistry*, 1988, **73**, 531-535.
20. A. Faes, A. Hessler-Wyser, A. Zryd and J. Van herle, *Membranes*, 2012, **2**, 585.
21. F. Millange, V. Caignaert, B. Domenges, B. Raveau and E. Suard, *Chemistry of Materials*, 1998, **10**, 1974-1983.
22. I. D. Brown and D. Altermatt, *Acta Crystallographica Section B*, 1985, **41**, 244-247.
23. J. P. Attfield, *Solid State Sciences*, 2006, **8**, 861-867.
24. A. J. Williams, J. P. Attfield and S. A. T. Redfern, *Physical Review B*, 2005, **72**, 184426.
25. P. Karen, P. M. Woodward, J. Lindén, T. Vogt, A. Studer and P. Fischer, *Physical Review B*, 2001, **64**, 214405.
26. T. Vogt, P. M. Woodward, P. Karen, B. A. Hunter, P. Henning and A. R. Moodenbaugh, *Physical Review Letters*, 2000, **84**, 2969-2972.
27. Y. Tomioka, A. Asamitsu, H. Kuwahara, Y. Moritomo, M. Kasai, R. Kumai and Y. Tokura, *Physica B: Condensed Matter*, 1997, **237–238**, 6-10.
28. Y. Tomioka, A. Asamitsu, Y. Moritomo, H. Kuwahara and Y. Tokura, *Physical Review Letters*, 1995, **74**, 5108-5111.
29. N. E. Brese and M. O'Keeffe, *Acta Crystallographica Section B*, 1991, **47**, 192-197.

30. H. Hayashi, T. Saitou, N. Maruyama, H. Inaba, K. Kawamura and M. Mori, *Solid State Ionics*, 2005, **176**, 613-619.
31. G. A. Tompsett, N. M. Sammes and O. Yamamoto, *Journal of the American Ceramic Society*, 1997, **80**, 3181-3186.
32. Z. Naiqing, S. Kening, Z. Derui and J. Dechang, *Journal of Rare Earths*, 2006, **24**, 90-92.
33. U. Yutaka and N. Tomohiko, *Journal of Physics: Condensed Matter*, 2004, **16**, S573.
34. C. Perca, L. Pinsard-Gaudart, A. Daoud-Aladine, M. T. Fernández-Díaz and J. Rodríguez-Carvajal, *Chemistry of Materials*, 2005, **17**, 1835-1843.
35. E. Castillo-Martínez, A. J. Williams and J. P. Attfield, *Journal of Solid State Chemistry*, 2006, **179**, 3505-3510.
36. V. Caignaert, F. Millange, B. Domenges, B. Raveau and E. Suard, *Chemistry of Materials*, 1999, **11**, 930-938.
37. R. D. Shannon, *Acta Crystallographica Section A*, 1976, **32**, 751-767.
38. M. Gilleßen, M. Lumeij, J. George, R. Stoffel, T. Motohashi, S. Kikkawa and R. Dronskowski, *Chemistry of Materials*, 2012, **24**, 1910-1916.